The Atacama Cosmology Telescope: Detection of Patchy Screening of the Cosmic Microwave Background

William R. Coulton[1,2] Theo Schutt[3,4,5] Abhishek S. Maniyar[3,4,5] Emmanuel Schaan[3,4] Rui An,[6] Zachary Atkins,[7] Nicholas Battaglia,[8] J Richard Bond,[9] Erminia Calabrese,[10] Steve K. Choi[11,8] Mark J. Devlin,[12] Adriaan J. Duivenvoorden,[13] Jo Dunkley,[7,14] Simone Ferraro,[15,16] Vera Gluscevic,[6] J. Colin Hill,[17,1] Matt Hilton,[18,19] Adam D. Hincks,[20,21] Arthur Kosowsky,[22] Darby Kramer,[23] Aleksandra Kusiak,[17] Adrien La Posta[24] Thibaut Louis,[25] Mathew S. Madhavacheril,[12] Gabriela A. Marques,[26,27] Fiona McCarthy,[28,1] Jeff McMahon,[29,30,31,32] Kavilan Moodley[33,19] Sigurd Naess[34] Lyman A. Page,[7] Bruce Partridge,[35] Frank J. Qu[28,2] Neelima Sehgal[36] Blake D. Sherwin,[28,37] Cristóbal Sifón[38] David N. Spergel,[1,14] Suzanne T. Staggs[7] Alexander Van Engelen,[23] Cristian Vargas[39] and Edward J. Wollack[40]

[1]Center for Computational Astrophysics, Flatiron Institute, 162 5th Avenue, New York, NY 10010 USA
[2]Kavli Institute for Cosmology Cambridge, Madingley Road, Cambridge CB3 0HA, UK
[3]SLAC National Accelerator Laboratory 2575 Sand Hill Road Menlo Park, California 94025, USA
[4]Kavli Institute for Particle Astrophysics and Cosmology,
382 Via Pueblo Mall Stanford, CA 94305-4060, USA
[5]Department of Physics, Stanford University, 382 Via Pueblo Mall, Stanford, CA 94305, USA
[6]Department of Physics and Astronomy, University of Southern California, Los Angeles, CA 90089, USA
[7]Joseph Henry Laboratories of Physics, Jadwin Hall,
Princeton University, Princeton, NJ, USA 08544
[8]Department of Astronomy, Cornell University, Ithaca, NY 14853, USA
[9]Canadian Institute for Theoretical Astrophysics,
University of Toronto, Toronto, ON, Canada M5S 3H8
[10]School of Physics and Astronomy, Cardiff University, The Parade, Cardiff, Wales CF24 3AA, UK
[11]Department of Physics, Cornell University, Ithaca, NY 14853, USA
[12]Department of Physics and Astronomy, University of Pennsylvania,
209 South 33rd Street, Philadelphia, PA, USA 19104
[13]Center for Computational Astrophysics, Flatiron Institute,
New York, NY 10010, USA, Joseph HenrLaboratories of Physics,
Jadwin Hall, Princeton University, Princeton, NJ, USA 08544
[14]Department of Astrophysical Sciences, Peyton Hall,
Princeton University, Princeton, NJ USA 08544
[15]Physics Division, Lawrence Berkeley National Laboratory, Berkeley, CA, USA
[16]Department of Physics, University of California, Berkeley, CA, USA 94720
[17]Department of Physics, Columbia University, New York, NY, USA
[18]Wits Centre for Astrophysics, School of Physics,
University of the Witwatersrand, Private Bag 3, 2050, Johannesburg, South Africa
[19]School of Mathematics, Statistics & Computer Science,
University of KwaZulu-Natal, Westville Campus, Durban 4041, South Africa
[20]David A. Dunlap Department of Astronomy & Astrophysics,
University of Toronto, 50 St. George St., Toronto ON M5S 3H4, Canada
[21]Specola Vaticana (Vatican Observatory), V-00120 Vatican City State
[22]Department of Physics and Astronomy, University of Pittsburgh, Pittsburgh PA 15260 USA
[23]School of Earth and Space Exploration, Arizona State University, Tempe, AZ, USA 85287
[24]University of Oxford, Denys Wilkinson Building, Keble Road, Oxford, OX1 3RH, UK
[25]Université Paris-Saclay, CNRS/IN2P3, IJCLab, 91405 Orsay, France
[26]Fermi National Accelerator Laboratory, P. O. Box 500, Batavia, IL 60510, USA
[27]Kavli Institute for Cosmological Physics, University of Chicago, Chicago, IL 60637, USA
[28]DAMTP, Centre for Mathematical Sciences, University of Cambridge, Wilberforce Road, Cambridge CB3 0WA, UK
[29]Kavli Institute for Cosmological Physics, University of Chicago, 5640 S. Ellis Ave., Chicago, IL 60637, USA
[30]Department of Astronomy and Astrophysics, University of Chicago, 5640 S. Ellis Ave., Chicago, IL 60637, USA
[31]Department of Physics, University of Chicago, Chicago, IL 60637, USA
[32]Enrico Fermi Institute, University of Chicago, Chicago, IL 60637, USA
[33]Astrophysics Research Centre, University of KwaZulu-Natal, Westville Campus, Durban 4041, South Africa
[34]Institute of Theoretical Astrophysics, University of Oslo, Norway
[35]Department of Physics and Astronomy, Haverford College, Haverford, PA, USA 19041
[36]Physics and Astronomy Department, Stony Brook University, Stony Brook, NY 11794
[37]Kavli Institute for Cosmology, University of Cambridge, Madingley Road, Cambridge CB3 0HA, UK
[38]Instituto de Física, Pontificia Universidad Católica de Valparaíso, Casilla 4059, Valparaíso, Chile

arXiv:2401.13033v1 [astro-ph.CO] 23 Jan 2024

[39] *Instituto de Astrofísica and Centro de Astro-Ingeniería,*
Facultad de Física, Pontificia Universidad Católica de Chile,
Av. Vicuña Mackenna 4860, 7820436 Macul, Santiago, Chile
[40] *NASA/Goddard Space Flight Center, Greenbelt, MD, USA 20771*
(Dated: January 25, 2024)

Spatial variations in the cosmic electron density after reionization generate cosmic microwave background anisotropies via Thomson scattering, a process known as the "patchy screening" effect. In this paper, we propose a new estimator for the patchy screening effect that is designed to mitigate biases from the dominant foreground signals. We use it to measure the cross-correlation between *unWISE* galaxies and patchy screening, the latter measured by the Atacama Cosmology Telescope and *Planck* satellite. We report the first detection of the patchy screening effect, with the statistical significance of the cross-correlation exceeding 7σ. This measurement directly probes the distribution of electrons around these galaxies and provides strong evidence that gas is more extended than the underlying dark matter. By comparing our measurements to electron profiles extracted from simulations, we demonstrate the power of these observations to constrain galaxy evolution models. Requiring only the 2D positions of objects and no individual redshifts or velocity estimates, this approach is complementary to existing gas probes, such as those based on the kinetic Sunyaev-Zeldovich effect.

INTRODUCTION

The distribution of gas throughout the Universe contains a wealth of information on the astrophysical processes governing the thermodynamics of the circumgalactic and intracluster media (ICM)[1–5]. It is also a key ingredient in cosmological analyses, especially galaxy weak lensing analyses as highlighted in e.g., Refs. [6, 7]. Whilst the properties of this gas in the centers of massive clusters have been well characterized by X-ray and thermal Sunyaev-Zeldovich (tSZ) measurements [e.g., 3, 8–13], the gas distribution in cluster outskirts and lower mass systems is less well understood. Recent measurements of the kinetic Sunyaev-Zeldovich (kSZ) effect offer one means of studying this gas [14–18]. In this work we explore a complementary approach based on the "patchy screening" effect which, like the "projected fields" kSZ estimator [19–21], does not require spectroscopic data.

Cosmic microwave background (CMB) photons are Thomson scattered by electrons encountered on their path from the surface of last scattering to the observer. This scattering damps the primary CMB anisotropies. The isotropic component scales with the optical depth to reionization and is one of the six ΛCDM parameters [22–25]. However, the damping is anisotropic as lines of sight with more (fewer) electrons will be more (less) suppressed, and thereby spatially modulates the underlying CMB anisotropies [26–33]. This effect is known as the "patchy screening" effect and, on small scales ($\theta \lesssim 1°$), the new anisotropies are

$$\Delta T^{\text{patchy screen}}(\mathbf{n}) = -\delta\tau(\mathbf{n})\Delta T^{\text{primary}}(\mathbf{n}), \quad (1)$$

where $\delta\tau(\mathbf{n})$ is the fluctuation in the optical depth to last scattering in direction $\mathbf{n}$ and $\Delta T^{\text{primary}}(\mathbf{n})$ is from the primordial CMB anisotropy in that direction. The physical intuition is that on small scales the primary CMB has no power, so patchy screening is simply the damping of the larger scale CMB fluctuations by the small scale

variations in τ. See Ref. [32, 33] or the Supplementary Material for more details.

Patchy screening is important during two epochs of the Universe: 1) during the reionization of the Universe, when the Universe has large spatial fluctuations in the cosmic ionization fraction, and 2) in the late-time Universe, when excesses in the density of electrons occur around gravitationally collapsed objects [e.g. 34–37]. The observational signature from the latter epoch is damping of the primary CMB anisotropies at a scale of a few arminutes. These anisotropies are well suited to studying the distribution of gas in the Universe as the damping is linearly proportional to the excess of electrons (for the typical small values of optical depths encountered). Thus, the angular size and damping amplitude characterize the projected gas profile. Patchy screening is complementary to the kinetic Sunyaev-Zeldovich (kSZ) effect, which arises from Thomson scattering of CMB photons off moving electrons. Both effects probe the optical depth, but with different weightings: patchy screening depends on the background primary CMB anisotropies whilst the kSZ effect depends on the line-of-sight velocity.

Measuring the late-time patchy screening signal requires two components: a precise measurement of the large scale CMB anisotropies, as a measure of the CMB before damping, and low-noise measurements of the new small scale anisotropies. Ground based CMB experiments, such as the Atacama Cosmology Telescope (ACT), South Pole Telescope, the Simons Observatory, CMB-HD, and CMB-S4 [38–42], are designed for the sensitivities and resolution necessary to provide the latter component. These experiments are complemented by the precise measures of large scale CMB anisotropies made by the *Planck* and *WMAP* satellites [43, 44]. Exploiting this synergy, we use data from *Planck* and ACT to measure patchy screening at small scales.

CMB experiments are only sensitive to the patchy

screening signal integrated along the line of sight. To understand the host mass and redshift dependence of the signal, we cross-correlate the CMB data with another tracer of the gas distribution [37]. If the second tracer is measured at high precision, then cross correlation based methods also provide a means of boosting the detectability of the patchy screening effect. In this work we cross correlate the ACT-*Planck* CMB measurements with galaxies in the *unWISE* catalog, using a stacking-based approach [45–47]. The *unWISE* galaxy catalog contains over 500 million galaxies as obtained from the extended observations of the Wide-field Infrared Survey Explorer (WISE) satellite [48, 49]. The high source number density of this catalog makes it ideal for studying the patchy screening signal.

CROSS-CORRELATION METHODOLOGY

A key challenge to detecting patchy screening is the host of other small-scale millimeter sky signals. These include emission from high redshift star-forming galaxies and radio galaxies, as well as CMB secondaries such as gravitational lensing, and the thermal and kinetic Sunyaev-Zeldovich effects [see e.g., 50, for a review]. These foreground signals are expected to be at least 30 times larger than the patchy screening signal and are spatially correlated with it. To avoid potential biases, we combine well-tested component-separation methods with a new estimator called the "sign estimator."

The sign estimator uses two parts to isolate the patchy screening effect: the first part is a map of the large scale CMB anisotropies, which quantifies how much damping can occur. Current multifrequency measurements, such as those from the *Planck* satellite, can be combined to produce a map of the large-scale anisotropies that is dominated by the primary CMB. The sign operation, a non-linear function which sets all pixels to ± 1, is applied to this map. This operation isolates the primary CMB, and eliminates contaminating signals, as the sign of each pixel of the map is set by the dominant component. The second part is to multiply this map by a map of the small scale CMB anisotropies. Except for the patchy screening effect, the sign of the primary CMB anisotropies is uncorrelated with the small scale sky signals; thus the foreground contribution will average to zero and leave the patchy screening. This robustness to foregrounds means that we can apply our estimator to maps containing bright contaminants without biases. The sign estimator trades optimality for increased immunity to foreground biases. This is one of several conservative choices made to ensure a robust detection. In the Supplementary Material we show how this approach is motivated by the squeezed limit of the standard quadratic estimator. An in-depth comparison of different patchy screening estimators, along with forecasts for current and future experiments, is given in Ref. [51].

We detect patchy screening via its correlation with the distribution of galaxies. Specifically, we apply the sign estimator to cutouts of the CMB data extracted at the location of known galaxies. These cutouts are then averaged together in a 2D stack. A detailed description of our methodology is provided in the Supplementary Material.

DATA SETS

The CMB data used in this work are the component-separated CMB maps obtained from combining data from the *Planck* satellite with data from ACT, as detailed in Ref. [52]. Here we briefly review the key products and refer the reader to Ref. [52] for more details.

The *Planck* satellite observed the full sky over four years with an angular resolution of $7.22'$ at 143 GHz [43]. The component-separated maps are constructed from the NPIPE *Planck* data release [53] and use data between 30 GHz and 545 GHz. These maps provide the large-scale CMB measurement; the small scales come from high resolution measurements of the millimeter sky by ACT. ACT observed around one third of the sky over the course of 15 years [54–62]. This work uses data from Data Release 4 (DR4) and Data Release 6 (DR6), which contains data from 2013-2023. It comprises observations at three frequencies: 98, 148, and 225 GHz (known as f090, f150, f220). At 148 GHz the ACT beam full-width-half-maximum (FWHM) is $1.4'$. Typical noise levels in the ACT maps are $13/12/48$ μK arcmin at f090/f150/f220. Atmospheric noise, primarily from the vibrational and rotational modes of water vapor, has a red spatial power spectrum and inhibits ACT from making observations of the large scale CMB anisotropies [63]. Thus the combination of *Planck* and ACT data is well suited to studying the patchy screening signal.

The ACT and *Planck* multifrequency observations are combined using a needlet internal linear combination (NILC) to produce a map isolating the CMB anisotropies. This CMB map is dominated by the primary CMB anisotropies on angular scales ranging from full-sky to a few arcminutes. The resulting map is convolved to a $1.6'$ FWHM Gaussian beam. The NILC map we use here was optimized to produce an unbiased CMB map with minimal "noise" variance, with noise defined to be all signals (sky or instrumental) that are not the component of interest [64, 65]. As discussed further in the Supplementary Material, the robustness of our measurement can be tested by making variants of the NILC maps. These variants are produced by either using only subsets of the data during the NILC process (if only one frequency is used the NILC method can be thought of as a means of coadding data) or by applying constraints to ensure that a known contaminant signal does not contribute to the map "noise." To achieve this latter goal,

Sample	Mean Redshift	Mean Halo Mass $(M_\odot/h)$	Source density (arcmin^{-2})
Blue	0.6	1.4×10^{13}	0.58
Green	1.1	1.3×10^{13}	0.32
Red	1.5	1.6×10^{13}	0.018

TABLE I. The key properties of the *unWISE* galaxies as measured by Refs [46, 68, 69]. The source density is computed after our catalog cuts (see Supplementary Material).
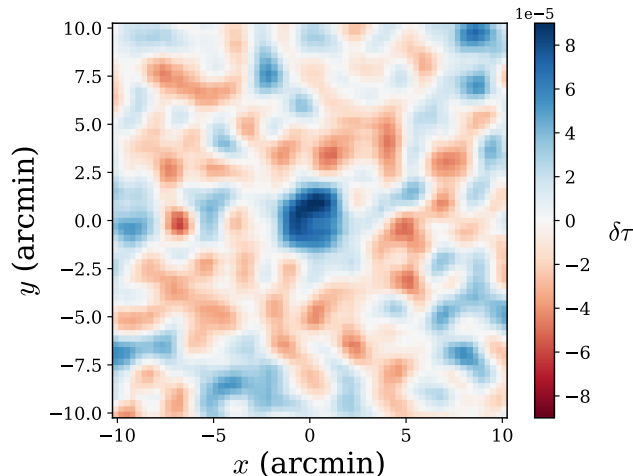
FIG. 1. High-pass filtered 2D stacked optical depth map, obtained by running the "sign" estimator on ACT data, at the positions of the *unWISE* blue sample. The optical depth map is convolved with the filter of Eq. (13), on top of the 1.6′ FWHM Gaussian ACT beam convolution. The visible excess in the center comes from the gas around the *unWISE* galaxies.

we use the constrained NILC method [66, 67].

The galaxy catalogs used in our cross correlation analysis come from the Wide-field Infrared Survey Explorer (WISE) satellite [48]. The WISE satellite observed the sky from 2010 to 2011 and then again from 2013 to the present. We use the "blue," "green" and "red" galaxy samples from Ref. [46] and refer the reader to Ref. [46] for details on the selection criteria. These samples, whose properties are summarized in Table I, are obtained from the deep 3.4 and 4.6 micron *unWISE* catalogs [49, 70, 71], with *Gaia* data used to help remove contaminant stars [72]. The high source densities and large overlap with ACT are the key reasons for using the *unWISE* catalogs – note that the patchy screening cross-correlation only needs the galaxy positions and not their redshifts.

In the Supplementary Materials we describe the simulations used to validate our analysis and to construct the covariance matrices used to interpret our results. We also detail a data-based test of the covariance matrix.
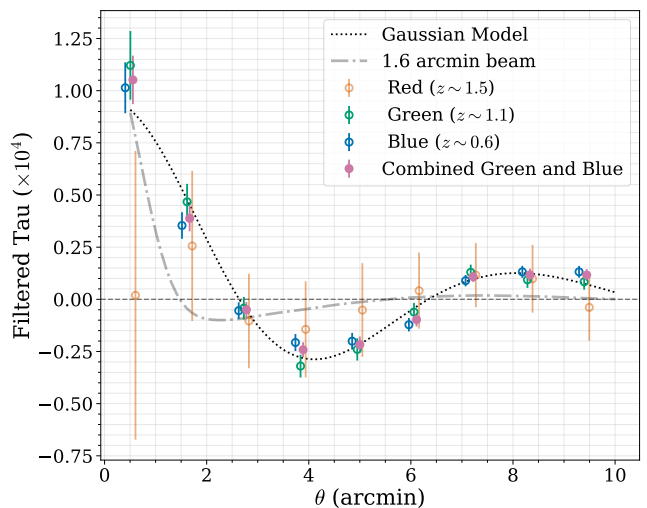

FIG. 2. Stacked 1D profiles of the optical depth, obtained from the sign estimator, Eq. (14), applied to filtered CMB data stacked at the locations of galaxies. The points show the measurements of the *unWISE* red, green, blue and combined blue-green samples. These are obtained by azimuthally averaging the 2D stacks. After accounting for the covariance of the points, the combined sample rejects the null hypothesis of no signal at $7.9\,\sigma$ (see Table II). The dot-dashed line is the signal for a point source and the dotted line is a Gaussian electron density profile, with parameters fit to the combined blue-green sample. The point-source and Gaussian profiles are convolved to the beam (1.6′ FWHM) and filtered in the same manner as the data. The error bars are computed from Monte-Carlo simulations as described in the Supplementary Material.

RESULTS

In Fig. 1 we present the 2D stack of the sign-weighted CMB data on the unWISE blue galaxies, where the patchy screening signal can be clearly seen. We show the azimuthally averaged 1D profiles of optical depth, computed with Eq. (14), for the three *unWISE* samples in Fig. 2. Whilst the highest redshift stack (red) is consistent with zero, we detect signals in the blue and green samples at high signal-to-noise ratio (SNR). This difference is expected given that the red catalog has an order of magnitude fewer members than either of the other catalogs. Note that the shape of the profiles, especially the "ringing" structure, arises from the filtering of the CMB map.

We compute the covariance of the data points, including the covariance between the green and blue samples, using Monte-Carlo simulations, described in the Supplementary Material. In Fig. 3 we show the correlation matrix for the blue and green samples. The strong radial correlations induced by the filtering can clearly be seen. These correlations are not due to the signal – the simulations do not include the patchy screening sig-
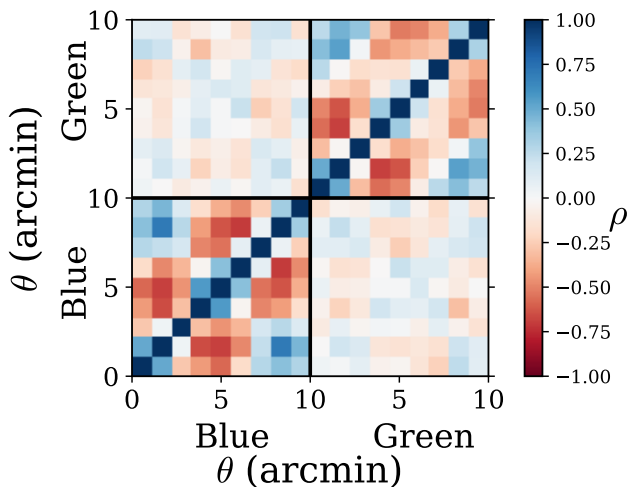
FIG. 3. The correlation matrices of the τ measurements from the *unWISE* blue and green samples, computed from 150 independent simulations that do not include the patchy screening signal. The lower left corner of the plot is the blue sample, the upper right is the green sample and the diagonals are the cross terms. Significant off-diagonal correlations arise from the high-pass filtering. No strong correlations are detected between the two samples.

nal – and arise from the primary CMB, noise and other sky components. These signal-free simulations quantify the expected noise-induced variance in the profiles. The comparison of our measurement to this noise quantifies the detection significance. The correlations between the two samples are consistent with noise. We combine the blue and green data points – with an inverse covariance weighting– to obtain a higher SNR sample, also shown in Fig. 2.

Table II provides χ^2 and p-values estimated from the data for two cases: the null hypothesis, and a two-parameter model described below. The large χ^2 values and low p-values for the null hypothesis demonstrate the high significance of the detection. The final column of Table II translates the p-values to the equivalent number of Gaussian sigmas, showing that the profile from the combination of the blue and green samples for the nine radial bins of Fig. 2 is inconsistent with the null hypothesis at 7.9σ. However, quantifying the detection significance from just the null hypothesis is non-trivial as the χ^2 values will clearly depend on the maximum radius used in the measurement. Note that if we just use three radial points we still reject the null hypothesis by more than 7σ.

We fit the data to a two-parameter model in order to perform a model comparison test to better assess the detection significance. In this phenomenological model the optical depth around the unWISE galaxies is modeled as a 2D symmetric Gaussian distribution. To this model we apply the CMB beam, filter in an identical manner
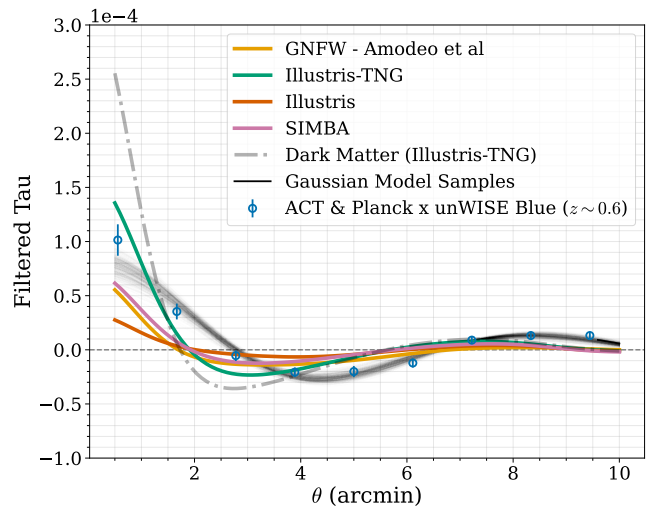

FIG. 4. A qualitative comparison of the measured profile from the blue sample to a set of theoretical models of the electron distribution: the Illustris (red), Illustris-TNG (green) and the SIMBA (purple) simulations, and the best-fit Generalized Navarro Frenk White profile from the kSZ analysis of BOSS galaxies[16] (orange). The dark matter profile from Illustris-TNG is shown in dot-dashed grey, re-normalized to match the integrated electron density. Each of the theoretical profiles has been filtered in a manner equivalent to the data. The black lines are samples from the fit to the Gaussian model. Perfect agreement between the data and simulations comparison is not expected as this comparison does not account for the observational selection function. The qualitative comparison already suggests that the gas does not follow the dark matter, and that future measurements will contain useful information about feedback and numerical simulations of galaxy formation [5].

to the data and compute the 1D azimuthal average; then we fit for the amplitude and width. The best fit profile is plotted in Fig. 2, and its χ^2 statistics are in Table II.

We consider two statistical tests to compare the Gaussian model to the null hypothesis: the Akaike Information Criterion (AIC) and an F-test [73–75]. Given the small size of data vector (9 elements), the Bayesian Information Criterion (a third commonly used model comparison metric) is effectively the same as the AIC discussed here and hence we only consider the AIC. We find AIC values of -39, -43 and -71 for the green, blue and combined samples respectively. These values correspond to strong evidence for the Gaussian model and hence strong evidence of a non zero signal. With the F-test we find p-values of $p = 0.003, 0.013$ and 0.0018, which also shows evidence for a non-zero signal model.

Discussion

Performing a quantitative interpretation of the measured gas profiles, in the vein of Ref. [16, 76], is challeng-

Rejection of null hypothesis			
Sample	χ^2_{null}	p-value	N_σ
Blue	67	6.8×10^{-11}	6.4
Green	53	2.2×10^{-8}	5.5
Red	3.5	0.93	-1.5
Combined blue and green	90	1.4×10^{-15}	7.9

Goodness of fit for the 2 parameter Gaussian model		
Sample	$\chi^2_{\text{best fit}}$	p-value
Blue	19	0.007
Green	11	0.16
Combined blue and green	15	0.04

TABLE II. The χ^2, p-values and equivalent Gaussian sigma significance (N_σ) of our measurements (top), and of fits with a Gaussian profile (bottom). Note that the statistics above used the full data covariance for the nine radial bins in each data set.

ing due to the large measurement errors and large uncertainties in the properties of the *unWISE* galaxies. We leave this challenge to future work, and restrict our analysis to qualitative comparisons. We contrast our measurements with a theoretical model and three state-of-the-art cosmological hydrodynamical simulations: Illustris [77], IllustrisTNG [78] and SIMBA[79]. Each simulation models the unresolved small-scale physics differently and the range provides some measure on the diversity of current theoretical predictions. For each simulation we follow the method of [80, 81] to compute the profiles. We use the *unWISE* properties from Ref. [68, 69] to perform the comparisons, with the mean redshifts and halo masses listed in Table I. For the simulations, we use the nearest redshift snapshot and a mass bin of $1.5 \times 10^{13} M_\odot/h \leq M_{\text{halo}} < 2.4 \times 10^{13} M_\odot/h$. We do not attempt to reproduce the *unWISE* sample selections, nor the impact of satellite galaxies, and therefore do not expect a perfect agreement.

First, we compare the measured profiles to the profile from a point source. Fig. 2 shows that our data strongly favours a more extended source for the signal. The electrons are not expected to be distributed as a point source. This comparison demonstrates that our measurements can probe the spatial distribution of the gas and provides a check on potential point source contamination. We then compare the measurements of the blue and green samples. From the fits to the samples' profiles, Fig. 2, we find that the green and blue sample profiles are fit by Gaussian models of widths $\theta_{\text{FWHM}} = 5.3 \pm 0.5$ and $\theta_{\text{FWHM}} = 5.7 \pm 0.5$ arcmin. Note that without evolution of profiles, the angular size of the green sample is expected to be smaller due to its higher redshift. These results highlight the potential of future, higher SNR measurements to characterize the redshift evolution of the distribution of gas.

Next we compare our measurements to the expected distribution of dark matter. As can be seen in Fig. 4, the measured gas profiles do not follow the dark matter (grey). Note that we show the dark matter from the Illustris-TNG simulation, but similar results are obtained from all three simulations. These results reproduce those seen in Refs [14–16, 76], which used kSZ measurements stacked on BOSS galaxies to demonstrate that the gas is significantly more extended than the dark matter. The best-fit generalized Navarro Frenk White (GNFW)[82] profile obtained from Ref. [16] is shown in orange. Our measurements are more consistent with [16] than the dark matter; however, our results appear to have a higher gas density and slightly more extended profile. The *unWISE* galaxies used in this work are different from the BOSS galaxies: the *unWISE* galaxies are infrared selected objects and trace star forming galaxies, whilst the BOSS galaxies are a constant stellar mass population and contain both star forming and quiescent galaxies [83]. Of particular relevance to this analysis is the proportion of galaxies that are central versus satellite members of their halos. The GNFW and simulation profiles do not account for the miscentering of the measured profiles that arises when we stack on satellite galaxies, which are offset from the center of the halo. The measurements from [68, 69, 84] suggest that the fraction of *unWISE* galaxies that are satellites is larger than in the BOSS sample. The impact of the satellite fraction on the observed profile is complex as it couples with the selection effects (see Ref. [85]) and can either broaden or sharpen the profile. These small-scale measurements of the gas around the unWISE galaxies complement the larger-scale kSZ-based measurements by [17] and future comparisons between screening and kSZ measurements will be a powerful astrophysical and cosmological probe.

Finally, we compare to electron density profiles from three state-of-the-art simulations. This qualitative comparison of the profiles, Fig. 4, shows that our measurements are broadly similar to all of the simulation suites. Better agreement is found with the SIMBA and Illustris-TNG simulations, which are known to have less heating and redistribution of the ICM than Illustris. Future measurements, with well-characterized galaxy samples, will enable quantitative comparisons and be highly informative for the next generation of hydrodynamical simulations.

In summary, CMB anisotropy data have reached the precision necessary to study the patchy screening effect. In this paper and Ref. [51], we introduce a new estimator that is robust to foreground biases, enabling the use of arcminue-scale temperature anisotropies with significant foreground contributions. A key feature of this analysis technique is that it relies only on the sky positions of galaxies, and thus complements existing methods of probing the gas distribution which also require galaxy distance estimates [14, 15, 76]. Our results already show

that patchy screening measurements provide a powerful method to characterize the physics governing the cosmic gas distribution. In Ref. [51], we show that future CMB observations with the Simons Observatory [40] and CMB-S4 [42] will allow the precision of these measurements to rapidly increase and greatly improve differentiation among galaxy formation models.

[1] J. P. Ostriker, P. Bode, and A. Babul, Astrophys. J.**634**, 964 (2005).
[2] D. Nagai, A. V. Kravtsov, and A. Vikhlinin, Astrophys. J.**668**, 1 (2007).
[3] B. R. McNamara and P. E. J. Nulsen, Annual Review of Astronomy and Astrophysics **45**, 117 (2007).
[4] N. Battaglia *et al.*, Astrophys. J.**725**, 91 (2010).
[5] E. Moser *et al.*, Astrophys. J.**933**, 133 (2022).
[6] A. Amon and G. Efstathiou, Mon. Not. R. Astron. Soc.**516**, 5355 (2022).
[7] G. Aricò *et al.*, arXiv e-prints arXiv:2303.05537 (2023).
[8] J. J. Ruan, M. McQuinn, and S. F. Anderson, Astrophys. J.**802**, 135 (2015).
[9] D. Crichton *et al.*, Mon. Not. R. Astron. Soc.**458**, 1478 (2016).
[10] A. de Graaff, Y.-C. Cai, C. Heymans, and J. A. Peacock, Astron. Astrophys.**624**, A48 (2019).
[11] D. Eckert *et al.*, Astron. Astrophys.**621**, A40 (2019).
[12] A. Zenteno *et al.*, Mon. Not. R. Astron. Soc.**495**, 705 (2020).
[13] S. Pandey *et al.*, Phys. Rev. D**105**, 123526 (2022).
[14] E. Schaan *et al.*, Phys. Rev. D**93**, 082002 (2016).
[15] E. Schaan *et al.*, Phys. Rev. D**103**, 063513 (2021).
[16] S. Amodeo *et al.*, Phys. Rev. D**103**, 063514 (2021).
[17] A. Kusiak *et al.*, Phys. Rev. D**104**, 043518 (2021).
[18] E. Schiappucci *et al.*, Phys. Rev. D**107**, 042004 (2023).
[19] O. Doré, J. F. Hennawi, and D. N. Spergel, Astrophys. J.**606**, 46 (2004).
[20] J. C. Hill *et al.*, Phys. Rev. Lett.**117**, 051301 (2016).
[21] S. Ferraro *et al.*, Phys. Rev. D**94**, 123526 (2016).
[22] Planck Collaboration Int. XLVI, Astron. Astrophys.**596**, A107 (2016).
[23] L. Pagano *et al.*, Astron. Astrophys.**635**, A99 (2020).
[24] Planck Collaboration Int. LVII, Astron. Astrophys.**643**, 42 (2020).
[25] R. de Belsunce, S. Gratton, W. Coulton, and G. Efstathiou, Mon. Not. R. Astron. Soc.**507**, 1072 (2021).
[26] J. P. Ostriker and E. T. Vishniac, Astrophys. J. Lett.**306**, L51 (1986).
[27] E. T. Vishniac, Astrophys. J.**322**, 597 (1987).
[28] W. Hu, D. Scott, and J. Silk, Phys. Rev. D**49**, 648 (1994).
[29] S. Dodelson and J. M. Jubas, Astrophys. J.**439**, 503 (1995).
[30] F. M. Persi, D. N. Spergel, R. Cen, and J. P. Ostriker, Astrophys. J.**442**, 1 (1995).
[31] A. Gruzinov and W. Hu, Astrophys. J.**508**, 435 (1998).
[32] C. Dvorkin, W. Hu, and K. M. Smith, Phys. Rev. D**79**, 107302 (2009).
[33] C. Dvorkin and K. M. Smith, Phys. Rev. D**79**, 043003 (2009).
[34] A. Roy, A. Lapi, D. Spergel, and C. Baccigalupi, J. Cosm. Astropart. Phys.**2018**, 014 (2018).
[35] C. Feng and G. Holder, Phys. Rev. D**99**, 123502 (2019).
[36] T. Namikawa *et al.*, Phys. Rev. D**104**, 063514 (2021).
[37] A. Roy, A. van Engelen, V. Gluscevic, and N. Battaglia, arXiv e-prints arXiv:2201.05076 (2022).
[38] B. A. Benson *et al.*, in *Millimeter, Submillimeter, and Far-Infrared Detectors and Instrumentation for Astronomy VII*, Vol. 9153 of *Society of Photo-Optical Instrumentation Engineers (SPIE) Conference Series*, edited by W. S. Holland and J. Zmuidzinas (PUBLISHER, ADDRESS, 2014), p. 91531P.
[39] S. W. Henderson *et al.*, Journal of Low Temperature Physics **184**, 772 (2016).
[40] P. Ade *et al.*, J. Cosm. Astropart. Phys.**2019**, 056 (2019).
[41] The CMB-HD Collaboration *et al.*, arXiv e-prints arXiv:2203.05728 (2022).

[42] K. N. Abazajian *et al.*, arXiv e-prints arXiv:1610.02743 (2016).

[43] Planck Collaboration I, Astron. Astrophys.**641**, A1 (2020).

[44] C. L. Bennett *et al.*, Astrophys. J. Suppl. Ser.**208**, 20 (2013).

[45] E. F. Schlafly, A. M. Meisner, and G. M. Green, Astrophys. J. Suppl. Ser.**240**, 30 (2019).

[46] A. Krolewski, S. Ferraro, E. F. Schlafly, and M. White, J. Cosm. Astropart. Phys.**2020**, 047 (2020).

[47] A. Krolewski, S. Ferraro, and M. White, J. Cosm. Astropart. Phys.**2021**, 028 (2021).

[48] E. L. Wright *et al.*, Astron. J.**140**, 1868 (2010).

[49] A. M. Meisner, D. Lang, and D. J. Schlegel, Research Notes of the American Astronomical Society **2**, 1 (2018).

[50] N. Aghanim, S. Majumdar, and J. Silk, Reports on Progress in Physics **71**, 066902 (2008).

[51] T. Schutt *et al.*, (in prep.).

[52] W. R. Coulton *et al.*, arXiv e-prints arXiv:2307.01258 (2023).

[53] Planck Collaboration *et al.*, Astron. Astrophys.**643**, A42 (2020).

[54] R. Dünner *et al.*, Astrophys. J.**762**, 10 (2013).

[55] J. Dunkley *et al.*, Astrophys. J.**739**, 52 (2011).

[56] S. Das *et al.*, Astrophys. J.**729**, 62 (2011).

[57] J. L. Sievers *et al.*, J. Cosm. Astropart. Phys.**2013**, 060 (2013).

[58] M. B. Gralla *et al.*, Astrophys. J.**893**, 104 (2020).

[59] T. Louis *et al.*, J. Cosm. Astropart. Phys.**2017**, 031 (2017).

[60] S. Naess *et al.*, J. Cosm. Astropart. Phys.**2014**, 007 (2014).

[61] S. Aiola *et al.*, J. Cosm. Astropart. Phys.**2020**, 047 (2020).

[62] S. Naess *et al.*, J. Cosm. Astropart. Phys.**2020**, 046 (2020).

[63] T. W. Morris *et al.*, Phys. Rev. D**105**, 042004 (2022).

[64] C. L. Bennett *et al.*, Astrophys. J. Lett.**396**, L7 (1992).

[65] C. L. Bennett *et al.*, Astrophys. J. Suppl. Ser.**148**, 97 (2003).

[66] X. Chen and E. L. Wright, Astrophys. J.**694**, 222 (2009).

[67] M. Remazeilles, J. Delabrouille, and J.-F. Cardoso, Mon. Not. R. Astron. Soc.**410**, 2481 (2011).

[68] A. Kusiak, B. Bolliet, A. Krolewski, and J. C. Hill, Phys. Rev. D**106**, 123517 (2022).

[69] A. Kusiak, K. M. Surrao, and J. C. Hill, arXiv e-prints arXiv:2303.08121 (2023).

[70] A. M. Meisner, D. Lang, and D. J. Schlegel, Astron. J.**153**, 38 (2017).

[71] A. M. Meisner, D. Lang, and D. J. Schlegel, Astron. J.**154**, 161 (2017).

[72] Gaia Collaboration *et al.*, Astron. Astrophys.**616**, A1 (2018).

[73] H. Akaike, in *Selected Papers of Hirotugu Akaike*, edited by E. Parzen, K. Tanabe, and G. Kitagawa (Springer New York, New York, NY, 1998), pp. 199–213.

[74] H. Akaike, IEEE Transactions on Automatic Control **19**, 716 (1974).

[75] D. Hahs-Vaughn and R. Lomax, *Statistical Concepts - A Second Course* (Routledge, London, 2012).

[76] M. Mallaby-Kay *et al.*, Phys. Rev. D**108**, 023516 (2023).

[77] D. Nelson *et al.*, Astronomy and Computing **13**, 12 (2015).

[78] D. Nelson *et al.*, Computational Astrophysics and Cosmology **6**, 2 (2019).

[79] R. Davé *et al.*, Mon. Not. R. Astron. Soc.**486**, 2827 (2019).

[80] L. Thiele *et al.*, Machine Learning: Science and Technology **3**, 035002 (2022).

[81] B. K. K. Lee, W. R. Coulton, L. Thiele, and S. Ho, Mon. Not. R. Astron. Soc.**517**, 420 (2022).

[82] J. F. Navarro, C. S. Frenk, and S. D. M. White, Astrophys. J.**462**, 563 (1996).

[83] K. S. Dawson *et al.*, Astron. J.**145**, 10 (2013).

[84] B. A. Reid *et al.*, Mon. Not. R. Astron. Soc.**444**, 476 (2014).

[85] B. Hadzhiyska *et al.*, arXiv e-prints arXiv:2305.00992 (2023).

[86] M. J. Mortonson and W. Hu, Astrophys. J.**657**, 1 (2007).

[87] O. Doré *et al.*, Phys. Rev. D**76**, 043002 (2007).

[88] M. Su *et al.*, arXiv e-prints arXiv:1106.4313 (2011).

[89] A. Roy *et al.*, J. Cosm. Astropart. Phys.**2021**, 003 (2021).

[90] F. Bianchini and M. Millea, Phys. Rev. D**107**, 043521 (2023).

[91] T. Namikawa, D. Hanson, and R. Takahashi, Mon. Not. R. Astron. Soc.**431**, 609 (2013).

[92] M. S. Madhavacheril and J. C. Hill, Phys. Rev. D**98**, 023534 (2018).

[93] E. Schaan and S. Ferraro, Phys. Rev. Lett.**122**, 181301 (2019).

[94] N. Sailer *et al.*, Phys. Rev. D**104**, 123514 (2021).

[95] O. Darwish *et al.*, arXiv e-prints arXiv:2111.00462 (2021).

[96] N. MacCrann *et al.*, arXiv e-prints arXiv:2304.05196 (2023).

[97] B. Horowitz, S. Ferraro, and B. D. Sherwin, Mon. Not. R. Astron. Soc.**485**, 3919 (2019).

[98] B. Hadzhiyska, B. D. Sherwin, M. Madhavacheril, and S. Ferraro, Phys. Rev. D**100**, 023547 (2019).

[99] F. J. Qu, A. Challinor, and B. D. Sherwin, Phys. Rev. D**108**, 063518 (2023).

[100] M. Hilton *et al.*, Astrophys. J. Suppl. Ser.**253**, 3 (2021).

[101] F. J. Qu *et al.*, arXiv e-prints arXiv:2304.05202 (2023).

[102] Our simulations showed that this source of bias is generally negligible, however we retain this cut out of an abundance of caution.

[103] G. Stein *et al.*, Journal of Cosmology and Astroparticle Physics **2020**, 012–012 (2020).

[104] N. Sehgal *et al.*, Astrophys. J.**709**, 920 (2010).

[105] Z. Atkins *et al.*, arXiv e-prints arXiv:2303.04180 (2023).

[106] R. Datta *et al.*, Journal of Low Temperature Physics **184**, 568 (2016).

[107] M. B. Gralla *et al.*, Astrophys. J.**893**, 104 (2020).

[108] M. Hilton *et al.*, Astrophys. J. Suppl. Ser.**235**, 20 (2018).

[109] W. Coulton, A. Miranthis, and A. Challinor, Mon. Not. R. Astron. Soc.**523**, 825 (2023).

[110] B. Stölzner, A. Cuoco, J. Lesgourgues, and M. Bilicki, Phys. Rev. D**97**, 063506 (2018).

[111] L. Amendola *et al.*, Living Reviews in Relativity **21**, 2 (2018).

[112] Planck Collaboration XXI, Astron. Astrophys.**594**, A21 (2016).

Supplementary Material

I. Overview of Patchy Screening Estimators

In this Section we first review the standard estimator as derived in Ref. [33] before presenting our new method. We refer the reader to Ref.[51] for a detailed analysis of the relative merits of the different estimators.

In the screening effect, free electrons along a given line of sight (LOS) Thomson scatter a fraction $1 - e^{-\tau}$ of the CMB photons from this LOS away from the observer. At the same time, Thomson scattering by the same free electrons deflects other CMB photons (which would not otherwise reach the observer) into the observer's LOS. Because Thomson scattering is a time-reversible process, the probability for a LOS photon to be deflected out of the LOS is the same as the probability for any photon to be deflected into the LOS. Thus screening is simply replacing a fraction $1 - e^{-\tau}$ of LOS photon flux at $\tilde{T}(\hat{n})$ with an equal fraction $1 - e^{-\tau}$ of all other photons incident on the electron, whose average temperature is $\bar{T}_{\mathrm{CMB}}$[33]:

$$T(\hat{n}) = \tilde{T}(\hat{n})e^{-\tau} + \bar{T}_{\mathrm{CMB}} \left[1 - e^{-\tau(\hat{n})}\right]. \tag{2}$$

This gives the observed temperature fluctuation:

$$
\begin{aligned}
\Delta T(\hat{n}) &\equiv T(\hat{n}) - \bar{T}_{\mathrm{CMB}} \\
&= \Delta \tilde{T}(\hat{n})e^{-\tau(\hat{n})} \quad \text{with } \Delta \tilde{T}(\hat{n}) \equiv \tilde{T}(\hat{n}) - \bar{T}_{\mathrm{CMB}}, \\
&= \Delta \tilde{T}(\hat{n})e^{-\bar{\tau}}e^{-\delta\tau(\hat{n})} \quad \text{with } \tau(\hat{n}) = \bar{\tau} + \delta\tau(\hat{n}), \\
&= \Delta T^{\mathrm{primary}}(\hat{n})e^{-\delta\tau(\hat{n})} \quad \text{with } \Delta T^{\mathrm{primary}}(\hat{n}) \equiv \Delta \tilde{T}(\hat{n})e^{-\bar{\tau}}, \\
&\simeq \Delta T^{\mathrm{primary}}(\hat{n})\left[1 - \delta\tau(\hat{n})\right].
\end{aligned}
\tag{3}
$$

Here we have introduced the average optical depth $\bar{\tau}$ to Thomson scattering, through which the primary fluctuations are observed ($\Delta T^{\mathrm{primary}}(\hat{n})$ versus the temperature fluctuations at the surface of last scattering $\Delta \tilde{T}(\hat{n})$). While this mean optical depth is not negligible ($\bar{\tau} \sim 5 - 6\%$ from Planck [22–25]) the fluctuations $\delta\tau(\hat{n})$ in the optical depth are much smaller, of order $10^{-5} - 10^{-3}$ for galaxy/cluster halos, justifying the linear expansion in the last line above.

Screening of the CMB also occurs in polarization. The equations above remain exact when replacing the temperature T by the Stokes parameters Q and U. In terms of E and B instead, the multiplication of Q and U with a scalar function $1 - \delta\tau(\hat{n})$ mixes E and B modes, thus leading to the generation of B-modes from E-modes [32–34, 86–89].

The quadratic estimator

As described in Ref. [33], we can construct a quadratic estimator for $\delta\tau$ as

$$\delta\tilde{\tau}(\mathbf{L}) = \int \frac{\mathrm{d}^2\boldsymbol{\ell}_1}{(2\pi)^2}\frac{\mathrm{d}^2\boldsymbol{\ell}_2}{(2\pi)^2} g(\boldsymbol{\ell}_1, \boldsymbol{\ell}_2) T(\boldsymbol{\ell}_1)T(\boldsymbol{\ell}_2)(2\pi)^2\delta^{(2)}(\mathbf{L} - \boldsymbol{\ell}_1 - \boldsymbol{\ell}_2) \tag{4}$$

where $T(\boldsymbol{\ell})$ are the 2D Fourier modes of the observed CMB temperature fluctuation map, as the intuition is clearer in the flat-sky approximation, and $g(\boldsymbol{\ell}_1, \boldsymbol{\ell}_2)$ are a set of weights. The weights are found by searching for the minimum variance unbiased estimator giving

$$\delta\tilde{\tau}(\mathbf{L}) = -\frac{1}{N_L} \int \frac{\mathrm{d}^2\boldsymbol{\ell}_1}{(2\pi)^2}\frac{\mathrm{d}^2\boldsymbol{\ell}_2}{(2\pi)^2} (2\pi)^2\delta^{(2)}(\mathbf{L} - \boldsymbol{\ell}_1 - \boldsymbol{\ell}_2)(C_{\ell_1}^{TT})\frac{T(\boldsymbol{\ell}_1)T(\boldsymbol{\ell}_2)}{C_{\boldsymbol{\ell}_1}^{\mathrm{tot}}C_{\boldsymbol{\ell}_2}^{\mathrm{tot}}}, \tag{5}$$

where C_ℓ^{TT} is the power spectrum of the $\tilde{T}(\mathbf{n})e^{-\bar{\tau}}$ field, i.e. the standard CMB power spectrum, C_ℓ^{tot} is the total power spectrum including foregrounds and instrumental noise and N_L is a normalization constant given by

$$N_L = 2 \int \frac{\mathrm{d}^2\boldsymbol{\ell}_1}{(2\pi)^2}\frac{\mathrm{d}^2\boldsymbol{\ell}_2}{(2\pi)^2} (2\pi)^2\delta^{(2)}(\mathbf{L} - \boldsymbol{\ell}_1 - \boldsymbol{\ell}_2)\frac{C_{\ell_1}^{TT\,2}}{C_{\boldsymbol{\ell}_1}^{\mathrm{tot}}C_{\boldsymbol{\ell}_2}^{\mathrm{tot}}}. \tag{6}$$

General small-scale τ estimator

For small scale reconstructions, $L \gtrsim 2000$, on data sets with noise and foregrounds, this can be approximated as

$$\delta\tilde{\tau}(\mathbf{L}) \approx -\int \mathrm{d}^2\mathbf{n}\, e^{i\mathbf{n}\cdot\mathbf{L}} T_{\text{large−scales}}(\mathbf{n}) \left[C^{-1}T_{\text{small−scales}}\right](\mathbf{n}) C_L^{\text{tot}} \left[\int_{\ell_{\text{small−scales}}} \frac{\mathrm{d}^2\boldsymbol{\ell}}{(2\pi)^2} C_\ell^{TT}\right]^{-1}, \tag{7}$$

where $T_{\text{large−scales}}(\mathbf{n})$ is a map that contains only the large-scale modes of the map, $\left[C^{-1}T_{\text{small−scales}}\right](\mathbf{n})$ is an inverse variance filtered map of small-scale modes and $\ell_{\text{small−scales}}$ are the modes that contribute to the small-scale map. This estimator arises from two parts: first the filter $C_\ell^{TT}/C_\ell^{\text{tot}}$ in Eq. (5) selects only modes where the CMB dominates. This filtering results in a map containing only large-scale modes. Second, the Dirac delta function in Eq. (5) forces the second part of the estimator to only select small-scale modes. Finally, we have approximated $C_{\boldsymbol{\ell}+\mathbf{L}}^{tot} \approx C_{\mathbf{L}}^{tot}$, which is valid on small scales where the power spectrum varies slowly. For the small-scale regime, these approximations will not significantly lose information compared to the full quadratic estimator or Bayesian estimators [90].

The key challenge on small scales is separating out this signal from other non-Gaussian sky components such as gravitational lensing, the thermal and kinetic Sunyaev-Zeldovich effects and the cosmic infrared background (CIB). These signals all produce quadratic couplings that will contribute to this estimator and can bias measurements of $\delta\tau$. In a manner analogous to lensing these can be removed by bias hardening the estimator [36, 91] and by using component separation techniques to remove signals with different spectral signatures (e.g. the tSZ and CIB)[69]. This approach will suppress these biases at the cost of reduced signal to noise. The difficulty for patchy screening is that the biases are much larger than the signal and so need to be suppressed to a very high degree. Fully removing similar biases to lensing estimators is very challenging [92–96] and it has yet to be demonstrated that such bias mitigation methods are sufficient for patchy screening analyses. This motivates the consideration of alternative estimators that are naturally robust to foreground biases.

By examining the structure of the small scale patchy screening effect

$$T(\mathbf{n}) \approx -T_{\text{large−scale}}(\mathbf{n})\delta\tau(\mathbf{n}), \tag{8}$$

it can be seen that an estimator for patchy screening can be obtained by replacing the $T_{\text{large−scale}}$ term in Eq. (7) with just the sign of the large scale mode and changing the normalization of the estimator. This gives the following estimator

$$\delta\tilde{\tau}(\mathbf{L}) \approx -\int \mathrm{d}^2\mathbf{n}\, e^{i\mathbf{n}\cdot\mathbf{L}} \,\text{Sign}\left[T_{\text{large−scales}}(\mathbf{n})\right] \left[C^{-1}T_{\text{small−scales}}\right](\mathbf{n}) C_L^{\text{tot}} \left[\langle|T_{\text{large−scales}}|\rangle\right]^{-1}, \tag{9}$$

where $\langle|T_{\text{large−scales}}|\rangle$ is the expectation of the modulus of the large scale field. It is straightforward to show that this estimator provides an unbiased estimator of the filtered τ field. Modes with wavelengths significantly larger than those in the small-scale field will not be recovered. Further, for small scale reconstructions the variance of this new estimator is only a factor of $\langle T_{\text{large−scales}}^2\rangle/\langle|T_{\text{large−scales}}|\rangle^2 = \pi/2$ larger. This result is obtained by evaluating the two expectations using a Gaussian distribution and using the relation

$$\langle|T|\rangle = \int_{-\infty}^{\infty} \mathrm{d}T\, |T|p(T) = 2\int_0^{\infty} \mathrm{d}T\, T p(T), \tag{10}$$

where $p(T)$ is the probability distribution of the temperature anisotropies. At the cost of this extra noise, this estimator suppresses all foreground biases. To understand why, note that the large scales of the CMB are dominated by the primary CMB anisotropies. By taking the sign of this fluctuation we isolate the primary CMB from the other contributions to the large scale CMB. This simple method removes almost all possible biases: biases such as the tSZ, CIB and kSZ are not correlated with the primary CMB so average to zero. A subtle bias could arise from correlations with the integrated Sachs-Wolfe (ISW) effect, which give a non-trivial contribution to the large scale modes. These can be removed by also removing the largest scale CMB modes ($\ell \lesssim 20$) or subtracting a map of the ISW field from the large scale leg. The latter approach is discussed in Section IV of the Supplementary Material.

Lensing is correlated with the large scale primary CMB; however this term also does not contribute to the estimator. To see this we first examine the effect of lensing on the small scales. This is given by

$$T(\mathbf{n}) = \tilde{T}\left(\mathbf{n} + \nabla\phi(\mathbf{n})\right) \approx \tilde{T}\left(\mathbf{n}\right) + \nabla\phi(\mathbf{n})\nabla\tilde{T}\left(\mathbf{n}\right), \tag{11}$$

where $\phi(\mathbf{n})$ is the lensing potential. As in the patchy screening case, the small scale lensing is given by the modulation of a large scale primary CMB term ($\nabla\tilde{T}$) by the small scale term (for lensing $\nabla\phi$). However lensing depends on the gradient of the large-scale CMB anisotropies, which is not correlated with the sign of the CMB anisotropy. Thus lensing also does not contribute to this estimator.

There are similarities between our estimator and the 'gradient inversion' lensing estimators [e.g. 97, 98]. However the gradient-inversion estimator generally increases the SNR of lensing reconstruction when lensing is dominant. This regime generally does not exist for the patchy screening estimator so we do not consider further dividing out the specific large scale mode, which would lead to the equivalent of the 'gradient inversion' estimator for patchy screening. Rather our estimator can be thought of as an analogy to the shear-only lensing estimators [93, 99]. We consider only part of the signal at the cost of signal to noise, but gain robustness to foreground emission. A detailed comparison of these different estimators is available in Ref. [51].

Implementation of the cross correlation estimator

To apply Eq. (9), we first need to create two filtered maps: one of the large-scale CMB anisotropies, and one of the small-scale CMB. For the low-pass maps we apply the following harmonic space filter, $f_\ell^{\text{low-pass}}$,

$$f_\ell^{\text{low-pass}} = \begin{cases} 1, & \text{if } \ell < 2000 \\ \cos\left(\frac{(\ell-2000)\pi}{300}\right) & \text{otherwise} \\ 0 & \text{if } \ell > 2150. \end{cases} \tag{12}$$

For the high-pass filter we use the following filter, $f_\ell^{\text{high-pass}}$,

$$f_\ell^{\text{high-pass}} = \begin{cases} 0 & \text{if } \ell < 2350 \\ \sin\left(\frac{(\ell-2350)\pi}{300}\right) & \text{otherwise} \\ 1 & \text{if } \ell > 2500. \end{cases} \tag{13}$$

The structure of the high- and low-pass filters was chosen to satisfy the following criteria. First, the low-pass map needs to contain enough modes to preserve the large scale sign. The fact that the CMB power spectrum is red means that this is satisfied providing the transition is above $\ell \sim 1000$. The location of the high-pass filter was chosen such that the power spectrum of the maps is approximately white (i.e. flat). When the power spectrum is white, Eq. (9) further simplifies as the harmonic-space, inverse-variance filter is just a constant and factorizes out. The smooth tapering of the filters prevents excess ringing from the harmonic space filtering. A separation between the two filters is used to prevent correlations between the high- and low-pass filtered maps. Moving the location, and width, of these filters by ± 250 was found to have minimal effect on the analysis. It is left to future work to optimize location of the filters, and widths of the transitions, which could be further optimized to maximize signal to noise.

Note that we do not deconvolve the beam from the scale-scale temperature map and instead include the beam and the impact of the filtering in our theory models. However, we do deconvolve the pixel window function, which would be difficult to account for in the theory model.

After the cuts described below, we extract a 20$\prime$ x 20$\prime$ cutout from the small scale map at the location of each *unWISE* galaxy. To account for sky curvature we use the tangent plane projection and interpolation methods described in Ref. [15]. We stack these cutouts, weighted by the sign of the large scale mode, as

$$\widehat{\delta\tau}^{\text{stacked}}(\mathbf{n}) = \frac{-\sum \text{Sign}[T^{\text{large-scale}}(\mathbf{n_o}+\mathbf{n})]T^{\text{small-scale}}(\mathbf{n_o}+\mathbf{n})}{N_{\text{objects}}\langle|T^{\text{large-scale}}|\rangle}, \tag{14}$$

where the sum is over objects at locations $\mathbf{n}_o$ and N_{objects} is the number of objects in the stack. We stack on tens of millions of galaxies for the blue and green samples; see Table I for source number densities. The sign of the large-scale field is consistent over $\sim 1/2\,\text{deg}^2$ patches. A 1D azimuthally averaged profile is computed from the stacks.

The non-linearity introduced by the sign operation suppresses foreground biases in the large scale map as the sign is determined by the primary CMB anisotropies. The immunity to foregrounds provided by the sign operation means we can include small scale temperature measurements, which are dominated by foregrounds, without becoming biased.

We do not stack on all the objects in the input catalog. Instead we perform a series of cuts to ensure that our results are robust. Whilst the foregrounds will average to zero over many objects, due to the sign weighting, for a finite number there can be a non-trivial residual [15]. To minimize the impact of especially bright objects skewing the average, we exclude regions from our maps where there are known point sources or clusters. Specifically we avoid stacking on objects that are within $6'$ of a detected SZ cluster (those in the updated Ref. [100] cluster catalog), $6'$ of a subtracted point source (those detected in any of the input maps with SNR> 5), $10'$ of the edge of the map and $12'$ of sources that are inpainted. The latter are a set of especially bright objects that are inpainted during the construction of the NILC maps and are described in Ref. [101].

Next, we ensure that in the stack there are exactly equal numbers of positively and negatively weighted regions. This helps further suppress the foreground emission and is implemented by selecting a random subsample. A heuristic of this can be understood by splitting the sky into two regions: areas where $\text{Sign}[T^{\text{large}-\text{scale}}(\mathbf{n_o})]$ is positive and areas where it is negative. Within each region foregrounds will not average down, and so contribute a bias given by the size of the average source present in the map, e.g., the average amplitude of a dusty galaxy or thermal SZ cluster. The average is obtained from many objects ($\sim 10^6$) and so will be similar in the positive and negative regions of the sky. Thus, the degree to which these foregrounds cancel in the final estimate is set by the difference in number of sources in the positive and negative regions of the sky. The large scale CMB has a large coherence scale ($\sim 1°$) so in any single sky realization there will be O(10000) independent positive and negative regions. The Poissionian-like scatter means we expect ~ 1 % more sources in one region than the other. Without explicitly balancing the number of sources in each region, the degree of cancellation will leave a ~ 1 % residual of the mean foreground signal. If we instead manually force the same number of sources in each region, the cancellation will only depend on the difference in the average residual in each region. This will be approximately $1/\sqrt{N_{\text{objects}}}$ and in our case this is expected to reduce the residual by more than an order of magnitude.

Finally we can apply cuts based on the amplitude of the large-scale field. The argument that the sign operation removes contaminants works only when the large scale is dominated by the CMB. Whilst this is generally true, there are regions of the sky where the primary CMB anisotropies are small and these patches could be dominated by foreground emission. To mitigate this as a source of potential contamination we exclude the regions of the sky where the large-scale temperature fluctuation is $\leq 40\,\mu\text{K}$, where tSZ and CIB emissions could potentially change the sign of the large-scale temperature. This threshold was based on the typical large scale variance of the tSZ and CIB in simulated maps.[102]

II. Validation with Simulations

To validate this approach we apply the method to non-Gaussian CMB sky simulations. The goal is to verify both that the other sky signals do not bias the estimator and that the estimator is able to recover the input signal. These tests are structured to approximate the sky as observed by ACT and *Planck* satellite so that they serve as a validation of the data analysis presented in the main text.

Simulation Properties

We consider two non-Gaussian sky simulations: the Websky [103] and the Sehgal et al. [104] simulations. Each simulation contains a range of correlated and non-Gaussian CMB secondary anisotropies including: the tSZ, kSZ, CIB, lensing and radio galaxies. Both simulations are dark matter only simulations with the secondary anisotropies then 'painted' on in post processing. As the two simulations use distinct methods and models for this painting procedure, they provide some measure of the theoretical uncertainty on the properties of the CMB secondaries. We use the rescaled Sehgal et al. simulations presented in Ref. [40] that have been adjusted to be consistent with recent measurements.

Using these simulations of the sky, we construct simulated observations that match the properties of the ACT and *Planck* data sets used in this work (see the main text for further details). These simulations match the instrumental properties including map noise, beams, and observation frequencies. We refer the reader to Ref. [105] and Appendix B of Ref. [52] for a thorough description of these simulations. We use the Needlet Internal Linear Combination (NILC) component separation pipeline, described in Ref. [52], to combine simulations of the individual observations into a map of the CMB anisotropies. Through this procedure we obtain maps with the appropriate levels of residual foregrounds that are present in the observations.

(a) Websky simulations
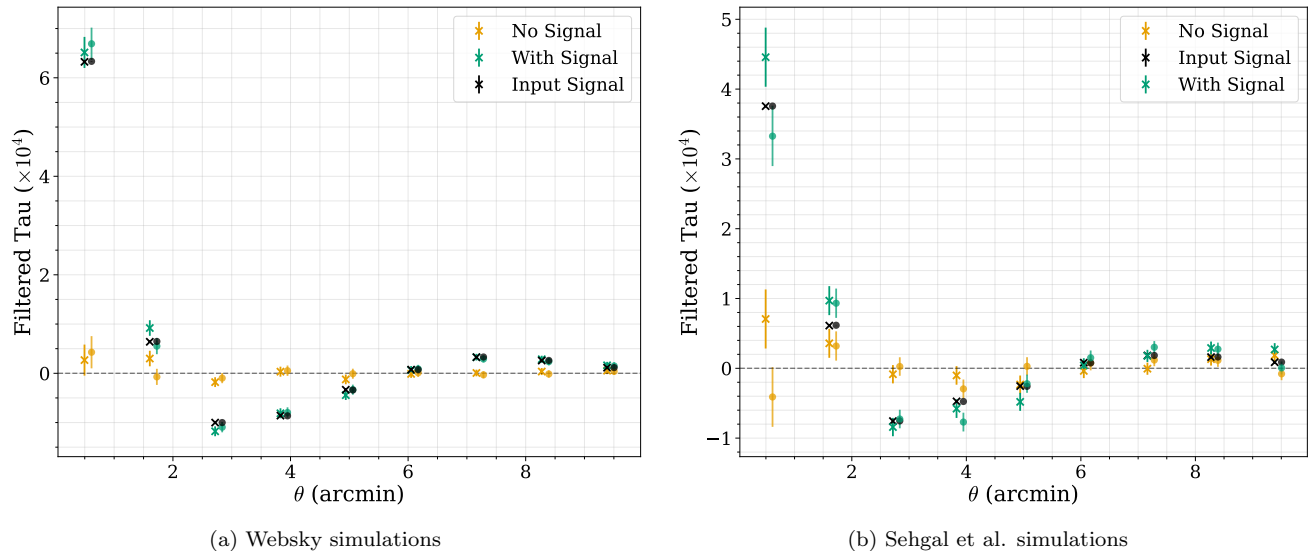
(b) Sehgal et al. simulations

FIG. 5. An application of our stacked estimator to mock ACT & *Planck* observations constructed from the Websky and Sehgal et al. simulations. The cross and circle points correspond to the two realizations. We apply the estimator to simulations that contain foregrounds but no patchy screening signal (blue lines). These are consistent with zero (see Table III) and demonstrate that our method is immune to foreground biases. We also show that the estimator is unbiased, as the measurements on simulations with a τ signal (orange) match the input signal when filtered in the same manner (green).

The Websky and Sehgal et al. simulations do not include any patchy screening signal. To validate that our method provides an unbiased measurement of non-zero signals, we created an additional version of the simulations that contain an approximate patchy screening signal. We first construct an approximate τ map, by rescaling the Compton-y map from each simulation by a constant factor to "convert" from Compton-y to optical depth. This factor is an approximation to the mean gas temperature of the halos and is chosen to give an average τ similar to the expected value ($\sim 5 \times 10^{-4}$). With this approximate τ map we create the patchy screening effect by using it to screen the primary CMB anisotropies, via Eq. (1).

The catalogs used in the stacking analysis are the halo catalogs of the two simulations. For the Websky simulations we use all halos with mass $M_h > 1.8 \times 10^{13}$ and in Sehgal et al. simulations we stack on all the available halos. Like the processing of the data, we avoid stacking on objects that are close to point sources, clusters or the edge of the mask. For the data the sources are identified in the maps using point source and cluster finders [e.g., 100, 106–108], however for the simulations we instead use the true source catalogs. The cut thresholds are set to approximately match the point source and cluster thresholds of the ACT data: CIB sources with amplitudes $\gtrsim 350\mu$ K (> 30 mJy) at 217 GHz, radio sources with amplitudes $\gtrsim 150\mu$ K (> 9 mJy) at 90 GHz and clusters with $M_{200} \gtrsim 5 \times 10^{14}$ M$_\odot$/h.

Analysis of the Simulations

In Fig. 5a and Fig. 5b we apply the method to the Websky and Sehgal et al. simulations. As can be seen when applied to the default simulations, those without any patchy screening signal, the estimator measurements are consistent with zero. This demonstrates that our method is not biased by the foregrounds present in these simulations. When applied to the simulations with a mock screening signal, we recover measurements that are consistent with the input τ signal. The oscillatory structure seen in the signal arises from the high-pass filtering performed on the small-scale CMB map.

These two tests provide evidence that our pipeline is able to provide robust and unbiased measurements of a patchy screening signal.
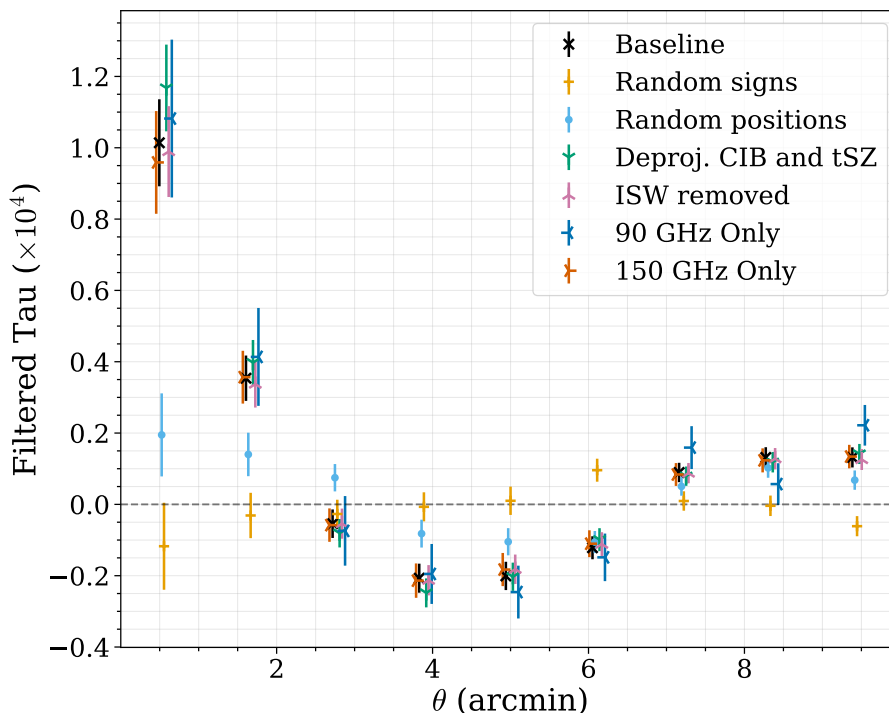
FIG. 6. A summary of the null and consistency tests performed to validate our result. The two null tests, stacking on random location and randomizing the sign used in the stack, are both consistent with zero and provide a data based check of our method (see Table III). The two foreground tests, which are labeled "Deproj CIB and tSZ" and "ISW removed", explicitly remove contamination from the tSZ, CIB and ISW effect. These demonstrate that our result likely contains no significant biases from these effects. The final tests, using only data from 93GHz or 148GHz, are consistent with anisotropies that have a blackbody spectrum, as expected for the patchy screening effect.

III. Uncertainty quantification

To compute the errors we generate a set of Gaussian simulations of the sky that match the properties of the sky. As the signal is highly subdominant to all the sky signals, we can simply treat the NILC map as a map of "noise." This is used as the input to the tiled noise model, described in Ref. [105]. With this formalism we can accurately capture the variation in the "noise" properties in both scale and location across the map. From these we generate an ensemble of 150 simulations. For each simulation we perform the same filtering as the data and then apply the stacked sign estimator at the locations of the *unWISE* galaxies. The weighting is given by the sign of a simulated large-scale CMB map. This is repeated over the ensemble of simulations to obtain an estimate of the covariance matrix.

As a cross check of this approach, we compute an approximate covariance matrix from the data themselves by computing the covariance matrix of the individual τ measurements from each galaxy. If each galaxy's profile were independent the covariance matrix of the stack would be $1/\sqrt{N_{\mathrm{objects}}}$ times the single galaxy covariance matrix. In practice the galaxies are not completely independent and thus this covariance matrix would slightly underestimate the true variance. We found that this approximate covariance matrix was in reasonable agreement with our simulated covariance matrix ($\sim 15\%$ agreement between the diagonal elements of the two matrices), providing a mild validation of our simulations.

IV. Robustness Tests

To validate our results we performed a series of data based robustness and null tests.

As a test of potential foreground biases, and of the computation of the covariance matrices, we performed two null tests. First we repeated our stacking analysis on random locations. Our estimator, Eq. (14), is not sensitive to the mean optical depth and so it is expected that if we stack on random locations we should see a signal consistent with

	χ^2	p-value	Equivalent Gaussian σ
Random positions	12	0.19	0.89
Random signs	13	0.16	0.98

TABLE III. The χ^2, p-values and equivalent Gaussian σ for two of the null tests.

zero. The number of locations is the same as the number in the original catalog, for which we use the largest sample, the blue sample. As seen in Fig. 6, when random locations are used, we find no signal. The χ^2 of this null test compared to zero, reported in Table III, is consistent with no signal. This tests both our estimator and the covariance matrices.

Second we repeat our stacking analysis, but randomize the sign used to weight each profile. This is a test of residual foreground components. Foregrounds are expected to average to zero in our standard estimator. However, if there are any anomalously large values they may average down very slowly and bias our result. This "random sign" test should identify such cases as randomizing the sign will remove the patchy screening signal. As seen in Fig. 6 and Table III, this null test is also consistent with no signal.

Next we perform tests aimed at identifying contamination in our measurement from two known sources: the thermal Sunyaev-Zeldovich effect (tSZ) and the cosmic infrared background (CIB). To test for biases from the tSZ and CIB, we make a constrained NILC map that explicitly removes the tSZ and CIB effects as described in Ref. [66, 67]. This map is referred to as the CIB and tSZ deprojected map and we refer the reader to [52] for a detailed description of our implementation. This operation results in a significant increase in the noise in the component-separated CMB map. We could deproject the tSZ and CIB separately. However as shown in [94, 109] removing only one component often increases the other component and so it is hard to predict how our results would change. However, on large scales the map is still dominated by CMB modes. To remove any biases from our measurement we note that we only need to ensure that the contamination is removed from one of the maps used in our estimator. In this case we can use the tSZ and CIB deprojected map as the low-pass filtered map for the sign operation. We make this choice as the scales relevant for the large-scale sign are largely unaffected by the increased noise in the deprojected map. The small scale noise is increased to such an extent that the signal to noise is too low for a useful consistency test. The resulting measurement, shown in Fig. 6, is consistent with our baseline measurement. This provides further support that our measurement is not contaminated by the tSZ or CIB.

We also check for contamination from the ISW effect, which leads to a bias that is not removed from our estimator. This is because the ISW contributes a significant amount of power to the CMB map and cannot be removed by multifrequency cleaning. This means that there may be regions where the sign is set by the ISW effect, not the CMB. The ISW effect traces the large scale potential field and so is correlated with other cosmic structures, such as the tSZ, CIB and *unWISE* galaxies, and thus could produce a signal in our analysis. It is expected that any bias from the ISW effect will be small as, even with optimal estimators, it is difficult to detect the ISW effect at high significance [110, 111]. To test for this we subtract the *Planck* collaboration's map of the ISW effect (see Ref. [112] for details of the construction of this map) from our component-separated CMB map. We then repeat our stacking analysis. By explicitly removing the ISW effect we should mitigate any potential bias. As shown in Fig. 6, our measurement is largely unchanged. This suggests that our measurement is not dominated by bias from the ISW effect. This null test has two limitations: first, it is difficult to produce a map of the ISW anisotropies. The map produced in Ref. [112] is noisy and not a perfect tracer of the true ISW effect. Thus our subtraction will not perfectly and noiselessly remove any biases. The ISW effect is only likely to bias our measurement on the largest scales, where it may impact the measured sign, and these are the scales where the ISW effect is best measured. Second, the ISW map has a slightly different mask compared to our fiducial analysis (see Fig. 20. of Ref. [112]). This will introduce some noise and scatter in our measurements. Given the very small impact of subtracting the ISW map, we expect both of these effects to be minor. An alternative method would be to filter out the largest scales. We do not consider that approach here as the filtering adds large amounts of noise to the sign measurement.

The final test performed is aimed at characterizing the spectral response of the observed signature signal. The frequency dependence of the patchy screening signal is expected to be the same as the primary CMB anisotropies. In the differential thermodynamic units used in this analysis, the anisotropies are expected to be the same size at all frequencies. We test this by generating maps that contain only observations at 93 GHz or 148 GHz. These maps are then high-pass filtered and used in the estimator. These two measurements will be consistent if the observed signal has no frequency dependence. We choose these two frequencies as they have sufficiently low noise and high resolution to obtain a high SNR measurement. Fig. 6 shows that these two measurements are consistent and thereby provides
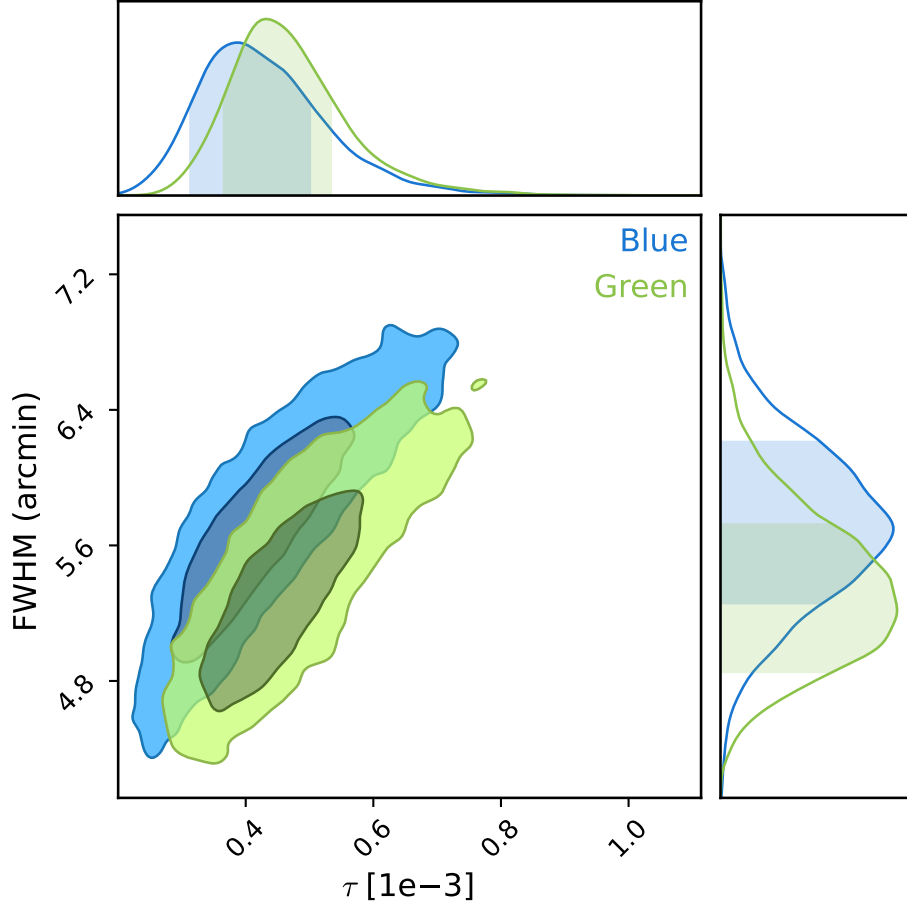
FIG. 7. Constraints on the central optical depth and Full-Width-Half-Maximum of the Gaussian profiles for the blue and green samples.

evidence that our observed signal has the expected frequency dependence.

V. Gaussian Profile Parameter Posteriors

In the main text, we use a Gaussian model to aid the quantification of the detection significance. We parameterized the Gaussian via the central amplitude τ and the FWHM. The Gaussian is then convolved with the beam and filtered in a manner identical to the data. In Fig. 7 we show the 2D contour plot for the best fit parameters of the Gaussian model fit to the green and blue samples. Whilst the exact degeneracy direction depends on the parameterization (instead of central optical depth, we could have considered the integrated optical depth), we find that both the amplitude and width are constrained. Note that the filtering leads to a complex interplay between the amplitude and width parameters. Filtering reduces the observed amplitude more significantly for wider profiles - a profile that is wider than the filtering scale is completely removed. This is discussed in detail in [51].